Nanoscale

Accepted Manuscript

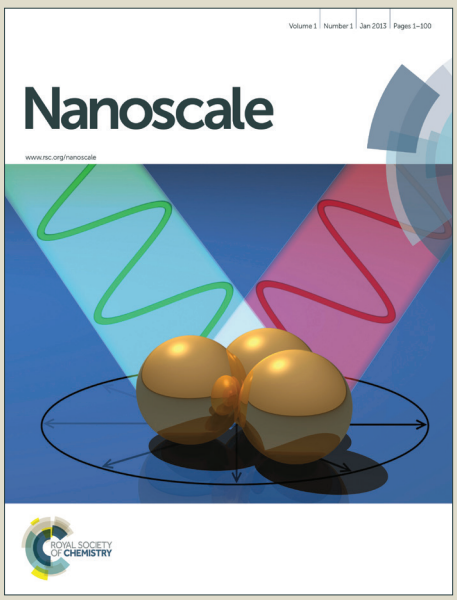

ROYAL SOCIETY OF CHEMISTRY

www.rsc.org/nanoscale

Journal Name

RSCPublishing

ARTICLE

Development of Highly Transparent Seedless ZnO Nanorods Engineered for Inverted Polymer Solar Cells

Swapnil B. Ambade[a], Rohan B. Ambade[a], Wonjoo Lee[b], Rajaram S. Mane[c], Sung Cheol Yoon[d]* and Soo-Hyoung Lee [a]*

Cite this: DOI: 10.1039/x0xx00000x

Received 00th January 2012,
Accepted 00th January 2012

DOI: 10.1039/x0xx00000x

www.rsc.org/

This work reports on inverted polymer solar cells (IPSCs) based on highly transparent (> 95 %), hydrophobic, seedless ZnO nanorods (NRs) as cathode buffers with extremely enhanced electrical characteristics. The transparent NRs suspension with stability for more than a year is achieved by adding a small amount of 2-(2-Methoxyethoxy) acetic acid (MEA). The ability of stable nanorod suspension to easily spin-coat is certainly an advance to fabricate films over large areas and to replace conventional seeding method to grow one-dimensional nanostructures for use in optoelectronic devices. We observe a strong correlation between the photovoltaic performance and the transparency of ZnO NRs. IPSCs using poly-3-hexylthiophene (P3HT) and [6, 6]-phenyl C_{60} butyric acid methyl ester ($PC_{60}BM$) mixtures in the active layer and transparent (MEA-capped) ZnO NRs as cathode buffers exhibit a power conversion efficiency of 3.24% under simulated AM 1.5G, 100mW.cm^{-2} illumination.

Introduction

The performance and function of energy-harvesting and electronic devices based on inorganic nanostructures depend critically on their architecture and morphology. Due to the hoping-free direct charge transportation, anisotropic nanomaterials such as oxidic nanorods (NRs) have found many applications in fabricating electronic, optoelectronic and electrochemical devices.[1-5] The role of oxide, which serves as a cathode buffer layer in the advanced energy conversion devices like inverted polymer solar cells (IPSCs), is typically to separate the donor: acceptor poly-3-hexylthiophene (P3HT) and [6, 6]-phenyl C_{60} butyric acid methyl ester ($PC_{60}BM$) active layer and the indium-tin-oxide (ITO) collecting electrode so as to prevent the possible recombination of positively charged holes in the active layer and the negatively charged electrons in the ITO film. [6-9] The use of one-dimensional (1D) oxide NRs with suitable lengths, for the buffer layer, can achieve solar cells with power conversion efficiency (PCE) higher than that obtained for the cell with a planar film buffer layer. The advantage of NRs compared with planar nanoparticles (NPs)-based film is that the NRs stretch into the polymers and may establish larger interfacial contacts with PCBM. Such a large interface between the polymer and the cathode buffer layer may facilitate the transfer of photogenerated electrons from the PCBM to the electron collecting electrode (i.e. ITO). Secondly, the higher charge mobility of oxide NRs than that of PCBM is another aspect that makes a contribution to the solar cell performance by improving electron collecting efficiency.

Moreover, 1D nanomaterials are known to have a lower trap density and unperturbed paths as a current-collecting electrode than (spherical) colloidal counterparts, and thus they are expected to facilitate smooth charge transfer. [2] Previous studies have shown that the electron transfer in solar cells with zinc oxide (ZnO) NRs is about two orders of magnitude faster than that with ZnO colloidal NPs. [10-13] The fact that oxides like ZnO can easily transfer electrons offer quite a prospect for their applications in hybrid optoelectronics.[14] Thus, there is a growing need for synthetic guidelines that need to be applied on the development of 1D nanomaterials. The practical requirements for development of 1D nanomaterials include morphology, dimensionality and orientation control, etc. Therefore, much emphasis has been placed on controlling the morphology of inorganic nanostructures during their growth processes.

We chose ZnO as a model metal oxide because 1D nanomaterials of semiconducting ZnO have found wide applications, such as in photonics, [15, 16] photovoltaics, [11, 17] piezoelectronics, etc. [18] As a demonstration of the versatility of ZnO, Tsukazaki *et al.* have shown that ZnO can be altered to transport holes as well as electrons, both essential attributes for optoelectronic devices. [19] From the perspective of synthesis, ZnO as a material offers immense ease and versatility, as it can be readily grown in solution. [20-22]The solution method has a unique advantage in large-scale synthesis of nanostructures at low-temperatures and low costs. This is in contrast to the high-temperature chemical vapor deposited ZnO nanostructures, which restricts the use of many commercially important flexible substrates. One such solution process for 1D ZnO growth is solvothermal chemical synthesis method, in which crystals form from a supersaturated aqueous solution. In a typical aqueous synthesis method, zinc salts are hydrolyzed in closed containers in the presence of weak polyamine bases for several hours, such as hexamethylenetetramine, producing ZnO nanowires (NWs), [23] NRs, [24] and even nanotubes (NTs) [25] or microtubes. [26] Nanostructure morphology is influenced by variations in reagent concentration, growth time and temperature, etc. [27] The solvothermal method, however, requires a prior ZnO seeding layer to initiate nucleation of ZnO, formed either chemically *via* spin-coating of zinc acetate dehydrate in an ethanol solution on the conducting substrate [17] or by applying few selective successive ionic layer adsorption

and reaction cycles [28] followed by annealing. As a result, the generation of seed layer involves additional fabrication step, where achieving uniformity and desired thickness possess quite a barrier. Moreover, the seeding method is too tedious considering the degree of control that needs to be executed, since; in this case growth density and dimensions of NRs have predominant dependence on the solution concentration, the growth time, or the thickness/size of the pre-deposited ZnO seed layer. [29-31] Also, the nature of the films obtained *via* a seeding process is non-transparent, milky and rough in appearance, resulting to limited light harvesting efficiency. For optoelectronic devices, one of the major pre-requisites is high transparency of oxidic cathode buffer in the visible region.

Thus, the development of a facile chemical method for the growth of transparent ZnO NRs over a wide range, that is free of seeding, remains a challenge. To overcome this impediment and to expand the simplicity of nano-chemical synthesis, strategies to employ novel synthesis routes that provide inexpensive, easy to carry out chemistry and high product yield are highly desirable. Moreover, as a pre-requisite of profitable application of new methods, it is to be ensured that the synthesis is carried out under mild reaction conditions, a research *niche* that we have savored over the years.[32]

This work reports a novel, simple and scalable strategy for developing clean, seed-layer-free and highly transparent ZnO planar NRs film for use as cathode buffer layer in polymer solar cells with inverted geometry. Our technique is based on spin coating of the pre-synthesized ZnO NRs on the pre-cleaned ITO substrate, the spinning rate is maintained to obtain buffer layer of desired thickness (~80 nm). Solution-based deposition techniques, like spin coating, are the most desirable processes as they are simple, cheap and large-area deposition methods. [33, 34]During spin-coating, phase separation sets in, and after evaporation of the solvent, lateral phase morphology is obtained. [35] This approach of direct spinning offers immense versatility to allow one-step production of oxidic nanomaterial's with excellent coating properties for applications that demand high transparency, uniformity at the minimum possible thickness and ultraclean surfaces.

Experimental

Synthetic Procedure

Planar ZnO NRs were synthesized by hydrolysis and condensations of zinc acetate dihydrate by NaOH in ethanol solvent. The synthesis conditions were adapted in order to control the desired morphology of the ZnO NRs with the much necessitated aspect ratio. The alkali solution of zinc to be solvothermally processed was prepared by dissolving molar ratio of Zn^{2+}: OH^- = 1:23 in pure ethanol (assay ≥ 99.9%). Prior to transferring to a teflon-lined autoclave, the solution mixture was homogeneously stirred for 15-20 minutes in the alcoholic medium ensuring no evaporation of alcohol. The solvothermal synthesis was carried out just close to the boiling point of water for maximum 4 h in an electric furnace ramped up and down at 4 ^oC/min. After the reaction, white crystalline products (ZnO NRs) were obtained. These crystallites were sequentially resuspended and washed with ethanol for several times to get rid of undesired salts that would be formed in the due course of reaction, most probably sodium acetate. After several washing steps in ethanol, the supernatant was decanted off carefully, ensuring only an exiguous amount of ethanol to remain in the solution. To this, ~1.5% (% v/v) chlorobenzene was introduced, prior to capping by MEA. The capping of ZnO NRs is a pivotal step and desires good controllability. The capping of ZnO NRs rapidly introduces hydroxyl groups (confirmed by Fourier transform infrared spectroscopy, FT-IR) without modifying the parent architecture of ZnO i.e. NRs, as depicted in Scheme 1. We speculate that a complex is formed between ZnO NRs and the OH^- present in MEA, which is an active site for bonding between MEA and ZnO NRs. This complex formed on ZnO NRs by capping of MEA certainly makes a strong polar interaction and makes ZnO NRs highly charged (confirmed by Zeta potential analysis, explained in ESI). These heavily charged ZnO NRs would provide a necessary driving force for charge percolation through them. Thus, the hydroxyl groups can be utilized as electronic anchors to effectively extract and transport charge carriers from the PCBM to the ITO electrode, by the virtue of its improved electrical conductivity. To achieve NRs with high purity and yield, an important point of consideration will always be skillful and meticulous pre-experimental conditions like selection of appropriate type of NaOH (e.g. in our experience, the dissolution of NaOH in ethanol was highly influenced by the diameter of the NaOH pellet), secondly, the degree to which maximum amount of ethanol be decanted-off and the degree of capping, to list a few.

Results and Discussion

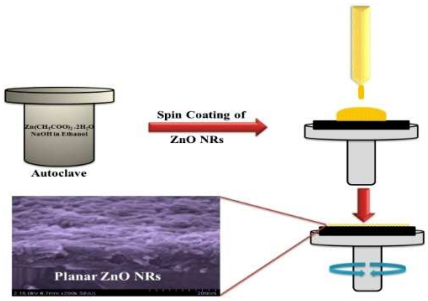

Scheme 1. Synthesis protocol for solvothermal synthesis of ZnO NRs.

A sharp diffraction arising at 2θ= 35.25° in the XRD pattern (see Figure S1 of Supporting Information (SI)) of capped ZnO reveal that the MEA appears to selectively cap the side facets of wurtzite ZnO, [36] allowing the growth to occur selectively only along the *c*-direction compared to uncapped ZnO. The intensities of (100) and (101) peaks in XRD spectra diminish significantly compared to (002) peak intensity after MEA capping revealing that MEA capping not only improves transparency (discussed later) of ZnO but also promotes the formation of unidirectional 1D structure, uncommon for seed-layer based ZnO NRs, which is one of the distinguishing features than previous reports.[17]The obtained strong near-UV emission peak of ZnO (Fig. 1a) centered at 362 nm is attributed to near band-edge transition of ZnO. Furthermore, a blue shift in wavelength of ~15 nm was observed for band-edge transition of capped ZnO. Generally, excess carriers through capping donated by MEA lead to the blue shift of optical band-to-band transitions of the MEA-capped ZnO. This is known as the Burstein–Moss (BM) effect, [37] where number of localized carrier density is responsible for blue shifting of absorption peaks. The blue shift of absorption peak strongly reveals that ZnO was well-modified by MEA. We believe, it is due to formation of transparent ZnO as transparent films are known to have comparatively less number of defect states/stacking faults as compared to that in opaque ZnO. In other words, Fermi energy level of opaque ZnO is at lower position compared to

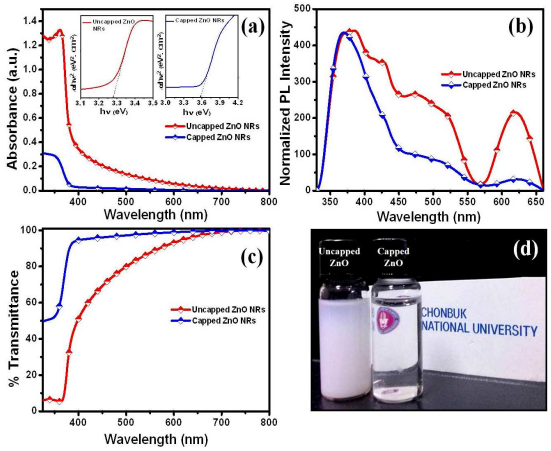

Fig. 1 (a) UV-vis, (b) PL, (c) UV–*vis* transmittance spectra of ZnO NRs films & (d) dispersion images (in vial) of uncapped and capped ZnO NRs.

transparent and functionalized one (as evidenced by Mott Schottky analyses presented further). The optical properties of ZnO were further studied by the room-temperature photoluminescence (PL) spectra under photon excitation of 325 nm. The PL spectrum of uncapped ZnO (Fig. 1b) consists of a near band-edge (NBE) at ~386 nm UV emission and a visible broad-band peak in the lower energy region, attributed to deep level emissions. The UV emission originates from the recombination of the free excitons of ZnO, while the visible emissions in the lower energy region probably results from either; (a) transition from conduction band (CB) to deep acceptor levels (O_i or O_{Zn}), (b) transition from deep donor levels (V_OZn_i) to valance band (VB), and (c) transition from shallow donor levels (Zn_i) to shallow acceptor levels (V_{Zn} and O_i), where V_{Zn} = vacant Zn, V_O = vacant O, Zn_i = interstitial Zn, O_i = interstitial O, V_OZn_i = complex of V_O and Zn_i, O_{Zn} = substitution of O at Zn sites. [38] After capped by MEA, the UV emission is blue shifted to 370 nm (consistent with optical studies), and becomes much stronger while the emission peak becomes weaker, resulting into significant increase in UV to visible ratio from 1.8 to 5.1. As explained by Bagnall *et al.* [39] the improvement of crystal quality (decrease of impurities, and structural defects such as oxygen vacancies) can cause a high NBE emission to deep-level emission ratio, resulting in detectable UV emissions at room temperature. The enhancement of UV emission clearly indicates the decrease in the probabilities of radiative trap recombination. Accordingly, it can be concluded that MEA strongly passivate oxygen vacancies at the surface of ZnO NRs on capping, ultimately resulting into good crystal quality.

The thin films of capped ZnO NRs appear transparent and absolutely uniform while that of uncapped ZnO NRs were opaque. Apart from the visual examination of the films, which gave a good estimate of its optical quality, transmittance measurement was used to characterize the films quantitatively. From the transmittance analysis, by using the *Swanepoel's envelope* method, [40] the calculated refractive index of capped ZnO was 1.79 which is close to the refractive index of ITO ($n \approx$ 1.8). Thus, there is no physical difference in the reflected light between the capped ZnO film coated and uncoated surfaces. In sharp contrast, the uncapped ZnO film appears opaque as the light strongly scatters off the ZnO that possessed a comparatively higher refractive index ($n \approx$ 2.42). On examining the % transmittance spectrum of both the films, a remarkable difference is detected (Fig. 1c). The thin film of capped ZnO showed average transmittance of more than 90% in the visible region, a significant enhancement in the light penetrating capability. Valley at 500 nm for capped ZnO is due to excitonic effect on account of its relatively higher transparency. The obtained high transmittance is one of the competitive values comparing with the results in previous synthesis of ZnO NRs. [41] In particular, for ZnO NRs grown on a seeded layer; it is highly challenging and intricate to achieve films with such high transparency and clarity. In the physical nature, transparency also occurs as a result of increased interactions offered by MEA capping on the surface of ZnO NRs. Simultaneously, as the interactions advance, the overdense ZnO NRs reach the criterion of transparency (i.e. effective nanostructure density lower than the uncapped ZnO NRs). This optically switches the ZnO from opaque to transparent and enables light propagation through the otherwise opaque, overdense ZnO film. Our University logo is clearly visible from the solution vial filled with capped ZnO NRs (Fig. 1d).

The field emission scanning electron microscopy (FE-SEM) images of capped and uncapped ZnO are shown in Fig. 2. In comparison to both the films, films of capped ZnO (Fig. 2b) showed much greater surface coverage on the substrate and uniformity than those of uncapped ZnO NRs (Fig. 2a), where majority of nanostructures seemed to have agglomerated. The high magnification images (Fig.2c, d) reveal that, in both cases, NRs of ZnO are parallel to substrate surface which is in contrast to previous results, indicating that in addition to transparent property, capped ZnO NRs provide planar structure and higher surface area than vertical. The planar ZnO NRs each of ~25 nm diameter and ~100 nm length are clearly seen in the high magnification images. The capped ZnO NRs (Fig. 2d) are morphologically similar to the ones observed prior to capping (Fig. 2c), although slightly longer, distinct and non-agglomerated. This is attributed to the meticulous control that we employ during the capping process. The varying ratios of Zn and O evidenced from EDS microanalysis (Fig. 2 e, f) confirms modification of ZnO after capping.

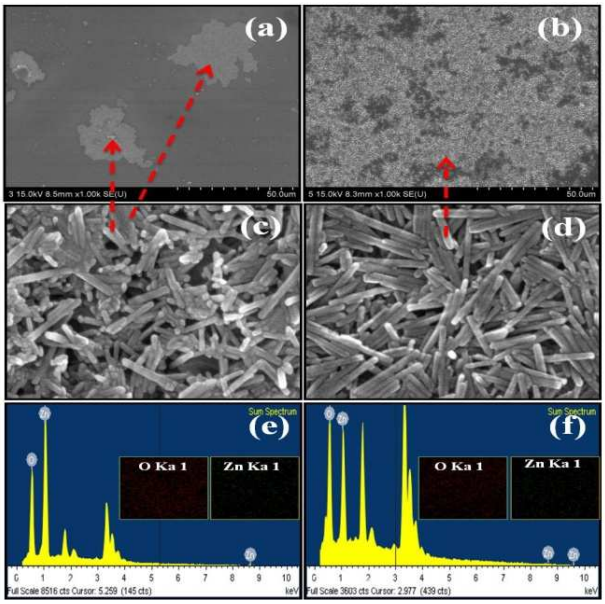

Fig. 2 (a-b) Low magnification, (c-d) High magnification FE-SEM images, (e-f) EDS spectra along with Zn & O mapping images (in the inset) of capped and uncapped ZnO NRs, respectively.

The Transmission electron microscopy (TEM) images also reveal that the geometrical shape of the ZnO nanostructures is rod-type (Fig. 3 a, b). Each nanorod has a uniform width along its entire length, and the typical widths of the NRs are in the range of 20 to 25 nm. The presence of some particles or much condensed NRs, (although very few in number) strongly suggests that the reaction is modulated by the diffusion limited Ostwald ripening, wherein large particles develop at the cost of smaller ones. Large particles are more energetically favorable. As the system tries to lower its overall energy, molecules on the surface of a small particle (energetically unfavorable, with only few bonded neighbors) will tend to detach from the particle, as per the Kelvin equation, and diffuse into the solution. When all small particles do this, it increases the concentration of free molecules in solution. When the free molecules in solution are supersaturated, the free molecules have a tendency to condense on the surface of larger particles. [42] Therefore, all smaller particles shrink, while larger particles grow, and overall the average size will increase. The inset in Fig. 3c shows a typical TEM image showing the presence of smaller nanocrystals on the side wall of an uncapped nanorod in the process of dissolution which supports the proposed growth mechanism. To further verify the morphological characteristic of the ZnO NRs, a cross-sectional TEM image taken from a nanorod is given in Fig. 3c, which exhibits a tubular-like cross-section. On transferring the NRs to an organic solvent (chlorobenzene) and capped further, the parent nanorods geometrical morphology was clearly maintained for our ZnO, albeit with a different crystallographic structure. The High resolution TEM (HRTEM) and the Selective area energy diffraction (SAED) measurements show that the ZnO NRs are structurally uniform and highly crystalline but with different growth directions, consistent to XRD results. The surface of the NRs appears clean, atomically sharp, and without any sheathed amorphous phase (Fig. 3e, f). An HRTEM image (inset of Fig. 3b) reveals that the capped ZnO NRs are single crystalline and dislocation free. The SAED pattern (Fig. 3f) indicates that the capped ZnO NRs have strong *c*-axis orientation, consistent with XRD findings. The lattice parameters were also calculated from the HRTEM. HRTEM of uncapped ZnO NRs (inset of Fig. 3a) reveal a superlattice structure of crystalline "stripes" with continuous and parallel crystallographic pattern. HRTEM image shows that the interplanar spacing of 4.5 Å between adjacent lattice planes corresponds to the distance between two [002] crystal planes; further proving [002] to be the preferred growth direction for the ZnO NRs. This [002] preferential NRs growth direction on the ITO substrate is also reflected in the XRD pattern, indicating excellent overall *c*-axis alignment of these NRs over a large substrate area. Based on the lattice image of [002] planes of capped ZnO NRs (inset of Fig. 3b), the interplanar spacing was found to increase by 0.7 Å supporting its different microstructure growth. The increased interplanar spacing in the capped ZnO NRs is believed to result from the electrostatic charge on the polar surfaces, which is disseminated by the anchoring of negatively charged hydroxyl ions. These parameters agree well with the reported values for [002] of wurtzite ZnO. [43] Additionally, the fringes are normal to the length of NRs which indeed is very significant for unhindered charge transport such that diffusion length is minimum, as the transportation takes place across the lengths of NRs. As a key feature, in both the ZnO, the fringes were parallel revealing no observation of any Frankel partial dislocation along the *c-axis*.[44-46]

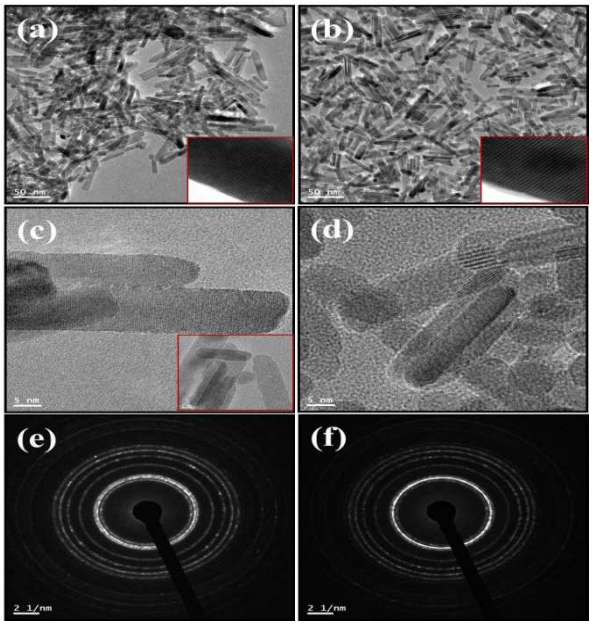

Fig. 3 TEM (a) & (b) Low magnification, (c) & (d) High magnification, (e) & (f) SAED pattern of uncapped and capped ZnO NRs, respectively. Insets: (a) & (b) corresponding HRTEM images exhibiting parallel fringes.

Experimental data from the FT-IR studies (see Fig. S2) carried out on both ZnO (uncapped and capped) under similar set of conditions clearly point to the hydroxylation of ZnO after capping. The chemical states of surface elements of both the samples were studied by XPS analysis. The Zn 2p core level spectra are presented in Fig. 4a, b. The Zn 2p spectrum of the uncapped ZnO NRs (Fig. 4a) shows two strong peaks centered at 1023.4 and 1046.4 eV, corresponding to Zn 2p3/2 and Zn 2p1/2, while those for capped ZnO NRs (Fig. 4b) were observed, respectively at comparatively lower binding energies, 1022.5 and 1045.5 eV. These values are in good agreement with the binding energies of Zn^{2+} ion. [47, 48] This clearly indicates that both the ZnO NRs have different chemical states despite of same morphology. Furthermore, the exact nature of chemical states responsible for modifying the surface of ZnO NRs was revealed by the O1s data of uncapped and capped ZnO NRs. High resolution O 1s spectrum as shown in Fig. 4c for the uncapped ZnO NRs shows a peak at 530.1 corresponding to lattice O^{2-} of ZnO. The next highest binding energy, centered at 532.1 ± 0.1eV, is attributed to adsorbed OH^- ($OH_{(ads)}$) located on the surface of ZnO. This peak is also observed at similar binding energy for the capped ZnO NRs, as shown in Fig. 4d. However, the O1s spectrum of the capped ZnO NRs does not show any peak related to lattice O^{2-} as in case of uncapped ZnO NRs. Instead this peak is shifted to relatively higher binding energy of 531.3 eV. A similar observation was also obtained previously by Grosvenor *et. al* [49] which they had attributed to the contributions of lattice OH^- species. The ratio of the hydroxyl oxygen to the lattice oxygen is as high as 0.77, indicating that ZnO NRs were strongly bound by OH^- groups. The XPS data of both Zn 2p and O1s provide strong evidence that ZnO NRs have been richly covered by OH^- groups with capping of MEA.

Typical resonance Raman spectra using solid state laser at 532 nm excitation are shown for the uncapped and capped ZnO NRs (Fig. 5). It appears from Fig. 5 that the Raman spectra exhibit only the longitudinal optical (*LO*) phonon and its

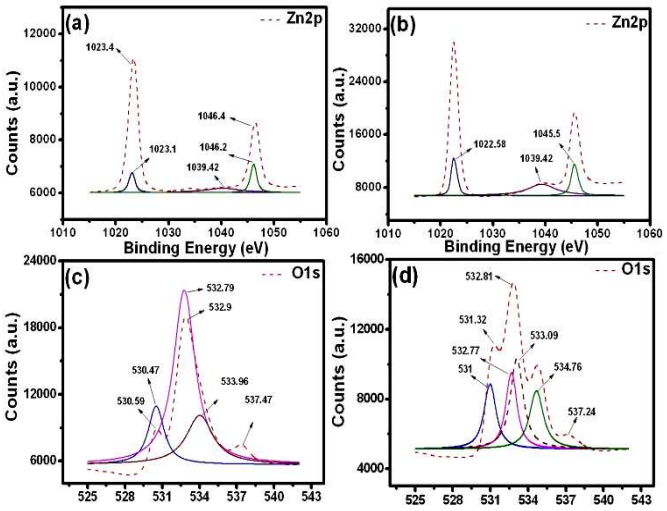

Fig. 4 (a), (b) Zn2p, (c), (d) O1s, XPS spectra of uncapped (left panel) and capped (right panel) ZnO NRs, respectively.

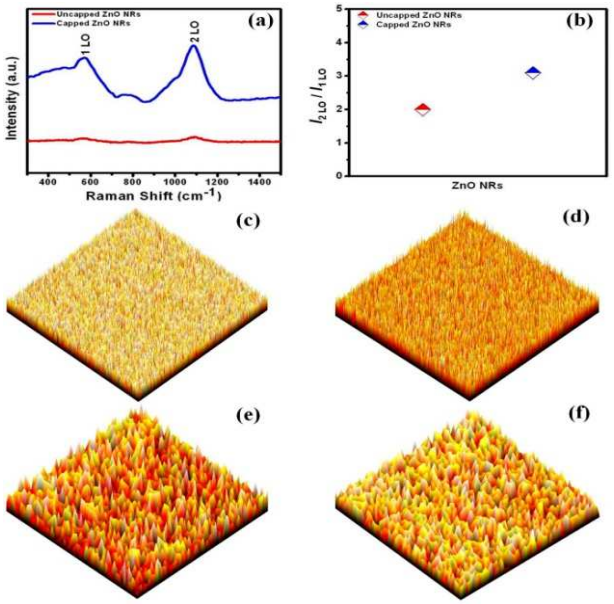

Fig. 5 (a) Raman Spectra for uncapped and capped ZnO NRs, (b) LO1 & LO2 Raman mapping of (c), (d) uncapped (e), (f) capped ZnO NRs at LO1 & LO2 positions, respectively.

overtones. The significant rise of intensity of the *LO* modes compared to the *E2* modes is attributed to the phenomena of interactions of the short ranged non-polar *E2* modes *via* the deformational potential, while the long ranged polar *LO* modes are also subjected to the incoming resonance effects with intermediate states due to *Frohlich* interaction. Thus, as the phonon energy gets closer to the free excitonic energy, the Raman scattering mechanism is mediated *via* a real excitonic state and exciton-phonon coupling results in the enhancement of scattering intensities of these LO modes and their higher overtones. As expected, owing to the fulfillment of resonance condition with 532 nm excitation, the LO mode around 576 cm^{-1} corresponding to *A*1 symmetry (*1 LO*) is observed for both uncapped and capped NRs. This is in well-accordance to previous observations. [50] Overtone modes up to higher order, (*2 LO*) are also observed in both cases confirming excellent crystalline quality of both NRs. [51] Higher intensity for the high order overtone modes in the capped ZnO NRs (blue spectrum in Fig. 5a) compared to the first order mode is due to the breakdown of symmetry rule at resonant condition and usually observed in samples with excellent crystalline order. Fig. 5b corresponds to the ratio of integrated intensities of 2LO to 1LO (I_{2LO}/I_{1LO}) for capped and uncapped ZnO NRs. The ratio of I_{2LO}/I_{1LO} depends on many factors such as the excitation energy, crystallite size, band gap energy, temperature, impurity concentration, and lattice defects, etc. As a consequence of quantum-confinement effect, [52] the ratio of I_{2LO}/I_{1LO} is usually less than unity, which is not the case in our ZnO NRs. Thus this ratio was found to be greater than one in both capped as well as uncapped samples. Within the Franck-Condon approximation, the relation between the intensity of the n^{th} phonon replica I_n and the main emission I_o is given by $I_n = Io.\ S^n e^{-S}/n!$, where, S is the Huang-Rhys parameter, which can also be used to assess the coupling strength of the electron-phonon interaction. [53]For $I_{2LO}/I_{1LO} > 1$, the value of S is expected to be greater than 2. It is seen that with capping, I_{2LO}/I_{1LO} increases; clearly suggesting the enhancement of the electron-phonon coupling strength. [54] This is clearly an evidence of improved crystal quality when the ZnO was capped. This corroborates the observations of XRD and HRTEM. Consequently, a decrease in S leads to a slight decrease in I_{2LO}/I_{1LO}, as observed in the uncapped ZnO NRs (Fig. 5b). The strong crystalline nature of capped ZnO NRs is also apparent from the Raman maps obtained at LO1 & 2 positions of both uncapped (Fig. 5c, d) and capped ZnO NRs (Fig. 5e, f).

Interface morphology plays an important role in both charge transport and collection in photovoltaic devices. Critical variation of interface morphology between the electron transport layer and active layer was observed after incorporating hydroxyl groups to the surface of ZnO NRs, as also evidenced from the XPS analysis (Fig. 4c, d). This modification resulted from MEA capping, enhanced the surface wettability of ZnO nanorods by making them more hydrophobic (contact angle~50^o), as shown in Fig. 6. Moreover, the charge reverses from plus to minus on capping, reversing the polarity of ZnO NRs, as evidenced by the zeta potential (ζ) studies (see Fig. S3). The observed negative potential of the hydrophobic capped ZnO NRs is consistent with previous findings. [55, 56] We attribute this change in polarity to the adsorption of anionic hydroxyl (OH^-) ions on the surface of ZnO NRs.

The local electronic behavior of the NRs was probed using the conducting probe atomic force microscopy (C-AFM). Using C-AFM, one can simultaneously measure topography and current distribution (conductivity) over the sample surface by

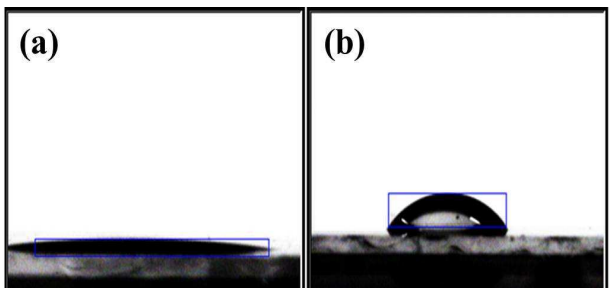

Fig. 6 Water contact angle measurements of a) uncapped and, b) capped ZnO NRs.

using the AFM tip as a nanometer-scale electrical probe, by applying the bias voltage between tip and sample surface to measure the tunneling current between the two. The current distribution maps (Fig. 7b, d) provide a clear estimation of charge transport capability of ZnO NRs in devices at the nano-scale. The bright (white) and dark (golden) spots indicate relatively high and low values, respectively, of current flow through the ZnO NRs. The current images obtained by applying -1V bias voltage (V_b), respectively, clearly show that the quantity of current flowing through the capped ZnO NRs is magnitudes higher than that in case of uncapped ZnO NRs. This observation reflects the increased surface conductivity of capped ZnO NRs due to charging by accumulation of OH^- ions on the outer as well as inner layers of ZnO NRs. [56] The surface topography reveals a highly contiguous and a uniform film of capped ZnO NRs (Fig. 7c) unlike of uncapped ZnO NRs (Fig. 7a) wherein, the film is not only non-uniform but also unstable where NRs tend to agglomerate. Thus, the C-AFM experiments clearly reveal that the films of uncapped ZnO NRs are poor conductors. The increased conductivity of capped ZnO NRs suggests that, on capping extra electrons are retained by the ZnO NRs. In semiconductors, the conductivity is enhanced as a result of strong confinement of a carrier in the nanostructure. As a result of capping to ZnO, the carrier leaks more into the crystallite surroundings of the ZnO NRs, indicating that many channels exist for charge transport. [14, 57]The higher and more uniform electron conduction in capped ZnO NRs obviously aid in improving the electron extraction when using capped ZnO NRs as cathode buffers in the IPSCs.

To verify the difference in cathode buffer layers, ultraviolet photoelectron spectroscopy (UPS) was carried out to investigate the energy levels of both the ZnO NRs. The high binding-energy cut off (E_{cutoff}) of both the ZnO is shown in Fig. 8. The valence band maximum (VBM) energy levels are calculated from the UPS data using the equation 1.

$$\text{VBM} = hv - (E_{cutoff} - E_{onset}) \quad (1)$$

where hv = 21.22 eV, is the incident photon energy, and E_{onset} is the onset relative to the Fermi level (EF) of Au (at 0 eV), where EF is determined from the Au substrate. From the UPS data, the calculated VBM values for uncapped and capped ZnO NRs are -7.69 and -7.53 eV, respectively. On the basis of these VBM energies and optical gaps obtained from the onset of absorption spectra, the estimated conduction band minimum (CBM) positions are -4.41 and -3.96 eV, respectively (see Table. 1 for energy levels of both the cathode buffers). The CBM of capped ZnO NRs is shifted by ~0.45 eV, ensuring a much lower energy barrier. A suitable CBM energy of cathode buffer allows much favorable band alignment to the lowest unoccupied molecular orbital (LUMO) level of the acceptor (PCBM), and would facilitate smooth electron collection/transport to ITO. Thus, it is expected to have large V_{OC} and J_{SC} from the IPSCs of capped ZnO NRs as there in considerable uplift in conduction band level compared to uncapped or bulk ZnO NRs. The energy levels of the IPSC components used are shown in Scheme 2.

To investigate the photovoltaic cell performance of ZnO NRs, we have chosen the most widely studied bulk-heterojunction system with inverted geometry as reference for this initial investigation, with P3HT as the donor polymer, and $PC_{60}BM$ as the small-molecule acceptor. The preparation of inverted structure solar cells (depicted in Scheme 2a) involved a spin coating of ZnO NRs (thickness~80 nm) on the ultraclean ITO glass substrate followed by spin coating of active polymers forming a bulk heterojunction, with subsequent coating of a hole transporting layer and finally a vacuum-deposition of thinner silver contact as the top electrode, forming a device with the ITO/ ZnO NRs/ P3HT: $PC_{60}BM$/ MoO_3/ Ag configuration (as depicted in Scheme 2), where the ZnO NRs

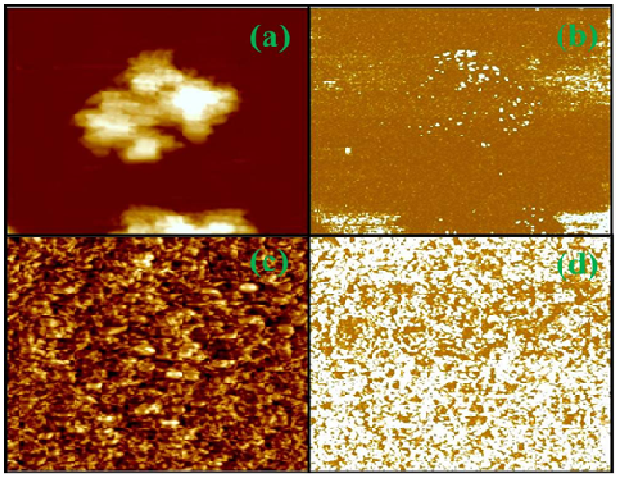

Fig. 7 Simultaneously recorded surface topography (a, c) and C-AFM current distribution maps (b, d) for uncapped and capped ZnO NRs films, respectively.

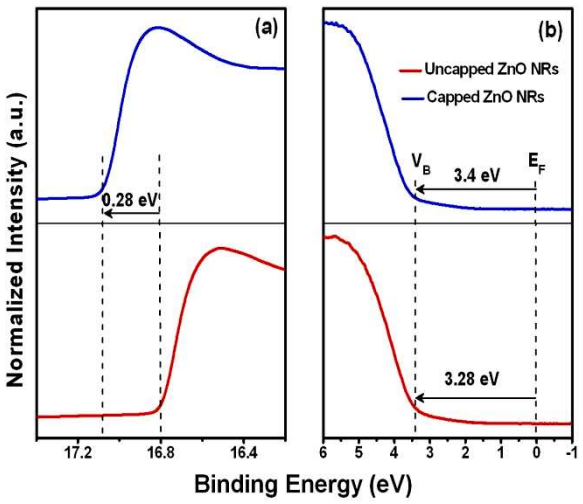

Fig. 8 UPS spectra of (a) the inelastic cut-off region and, (b) the VBM (onset) region of uncapped and capped ZnO NRs.

Table 1. Energy levels of planar ZnO NRs cathode buffer layer

ZnO NRs	$E_{\text{cut-off}}$ (eV)	E_{onset} (eV)	VBM (eV)	CBM (eV)
Uncapped	16.8	3.28	-7.69	-4.41
Capped	17.08	3.4	-7.53	-3.96

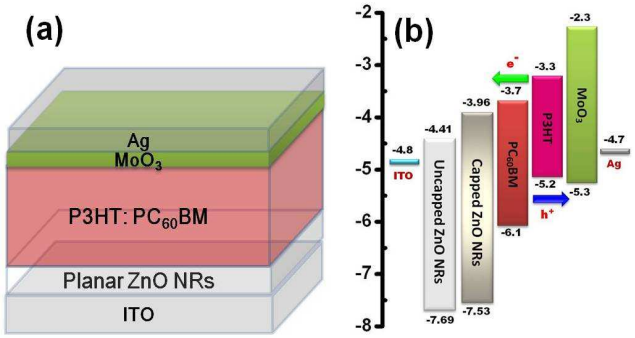

Scheme 2. (a) Device architecture illustration of the IPSCs fabricated in this study. (b) Energy level diagram of the IPSCs using uncapped and capped ZnO NRs as cathode buffer layers.

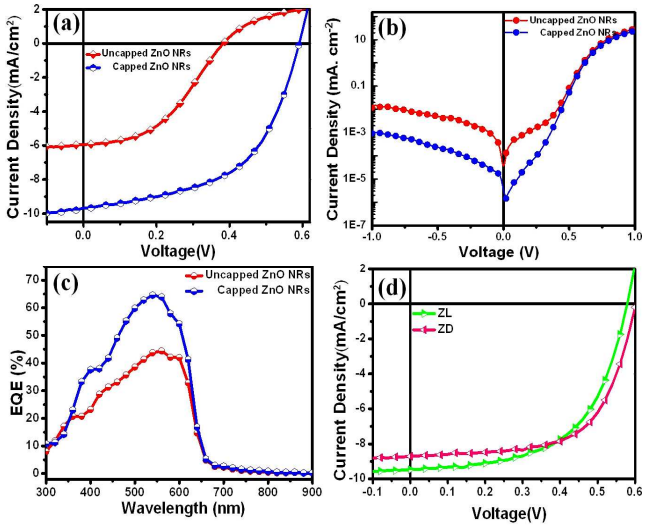

Fig. 9 Photovoltaic characterizations of IPSCs: *J-V* under (a) illumination, (b) dark (c) % EQE, (d) *J-V* curves of IPSCs consisting cathode-buffers of capped ZnO NRs synthesized from scale-up (ZL) batch & ZnO NRs that were preserved for 400 days (ZD).

served as cathode buffer layers, P3HT and $PC_{60}BM$ were the electron-donor and electron-acceptor, respectively, Mo_3O_4 was a hole transporting layer, and Ag was the top contact electrode. During fabrication, the P3HT:$PC_{60}BM$ active layer was achieved by spin-coating a 1:1 ratio mixture solution in 1, 2-dichlorobenzene. On spin coating ZnO NRs, the organics present in the ZnO NRs as a part of synthesis were allowed to evaporate by subjecting the ZnO NRs coated samples to open-air thermal treatment of 270°C for 10 min (optimized conditions). Furthermore, the phase separation in P3HT and $PC_{60}BM$ was achieved by solvent evaporation in vacuum for 12 h. Finally, the samples were vacuum evaporated to deposit hole-transporting layer to optimized thickness of 15nm prior to the deposition of Ag electrode. For comparison, another device was fabricated with the same configuration but using a substrate coated with ZnO NRs that were taken *in-situ* from the solvothermal autoclave at the end of reaction and void of any further surface modification (uncapped ZnO NRs).

The photovoltaic behavior of our ZnO NRs as cathode buffer layers employed in IPSCs is presented in Fig. 9. The current density-voltage (*J-V*) characteristics for both the devices under simulated 1 sun AM 1.5G illumination (Fig. 9a) and in dark (Fig. 9b) show that both the devices behave as a rectifying diode with significantly notable photovoltaic response for the device employing capped ZnO NRs as a cathode buffer layer. On incorporating capping to ZnO NRs, the photovoltaic parameters were enhanced dramatically. With short-circuit current density (J_{sc}) of 9.64 mA.cm^{-2}, open circuit voltage (V_{oc}) of 0.6 V, and fill factor (*ff*) of 56 %, an enhancement of approximately 159, 157 & 169% was observed respectively, in J_{sc}, V_{oc} and *ff*, of the IPSCs employing capped ZnO NRs as a cathode buffer layer, which resulted into PCE of 3.24%.

Without capping, a significant amount of charge leaks through the uncapped ZnO NRs, as evidenced from the dark current (Fig. 9b). Charge runs far too effective through the buffer layer when an uncapped ZnO NRs buffer layer was replaced by the capped ZnO NRs. Lower V_{oc} and *ff* in case of uncapped ZnO buffer layer can be attributed to parasitic leakage currents[58] caused by film defects and low charge mobility of highly dense and opaque ZnO NRs. Moreover, IPSCs with uncapped ZnO NRs as buffer layer exhibit a slightly S-shaped curve. This 'kink' in the *J-V* curve (Fig. 9a) arise due to presence of large interfacial energy steps or low mobilities and a reduction of the V_{oc} and crossing of the light and dark current curves when interfacial recombination is strong.[59] For very low mobilities, a space charge is built up in the device, because electrons and holes cannot be extracted sufficiently fast. Their concentration at the D/A interface is increased and hence recombination probability as well, which leads to a lower *ff*. The space charge built-up in the device results into reduction in the field. With decreasing field, the electrons start to pile up at the D/A interface. This obviously increases the recombination such that the *J-V* curve approaches the low mobility curve resulting into *S*-kink.

Additionally, the series resistance (R_s) of the device, which is defined by the slope of the *J-V* curve under illumination, substantially decreased for capped ZnO NRs device (13 Ω. cm^2) compared to that of uncapped ZnO NRs buffer layer device (79 Ω. cm^2), suggesting that the capped ZnO NRs is highly capable of reducing contact resistance to facilitate percolation of electrons across the device. This observation is demonstrated by the increased J_{sc} in the ZnO NRs capped device. This is very much attributed to the enhancement in the electrical conductivity of capped ZnO NRs (as strongly evidenced by C-AFM results). Higher conductibility ensures improved charge transport by compromising on exciton recombination that determines the V_{oc} of bulk-heterojunction PSCs. [60] Thus, a higher V_{oc} is yielded for inverted solar cells with capped ZnO NRs buffer layer. Furthermore, inverted solar cell device with capped ZnO NRs, showed a reduction in dark current under reverse bias (Fig. 9b). This result suggests that the capped ZnO NRs effectively passivate the local shunts at the ZnO interface, thereby blocking the injection of holes in the leakage pathways of the ZnO. The shunt resistance (R_{sh}) of the cell with capped ZnO NRs was found to be 1024 Ω. cm^2 in contrast to a drastically lower R_{sh} of 107 Ω. cm^2 for the uncapped ZnO NRs buffer layer cells, permitting charges to follow across the device rather than external load. The *J-V* measurements revealed that hydroxylates anchored to ZnO NRs acted as excellent electrical bridge between the NRs. The more uniform capped ZnO layer thus formed a better contact, with a higher *ff* due to reduced series resistance and increased shunt resistance, resulting an overall PCE of 3.24%. It is to be highlighted that the PCE reported in this work is the highest so

Table 2. Photovoltaic parameters of IPSCs containing uncapped and capped planar ZnO NRs as cathode buffer layer

ZnO NRs	J_{sc} (mA.cm^{-2})[a]	*Voc* (V)[a]	*ff* (%)[a]	*PCE* (%)[a]
Uncapped	**6.03** (5.82)	**0.38** (0.37)	**33** (32.40)	**0.75** (0.71)
Capped	**9.64** (9.58)	**0.60** (0.60)	**56** (55.80)	**3.24** (3.21)

[a]Average values are in parentheses.

far for the type of cathode-buffer (planar ZnO NRs) used in IPSCs. [61, 62] Moreover, this performance was also superior to the reference devices fabricated using sol-gel ZnO and ZnO nanoparticles (both annealed at 300 ^{o} C) as cathode buffer layers (see Figure S6-S7 of Supporting Information (SI))

A direct comparison of external quantum efficiencies in the organic solar cells with inverted geometry containing uncapped and capped ZnO NRs as cathode-buffer layers (Fig. 9c) shows a significant enhancement in extraction and transport of charge carriers in the case of capped ZnO NRs, an enhancement due solely to the presence of charge transfer interface within the device. After absorption and charge transfer, majority electrons in the $PC_{60}BM$ were effectively transported towards the ITO by the capped ZnO NRs simultaneously blocking the holes that might diffuse into the ITO. This is because, the capped ZnO NRs aid in effective separation of electrons and holes across the interface that enhances the effective driving force for charge extraction while reducing the likelihood of excitonic recombination. In order to assess the stability of capping groups on ZnO NRs, we fabricated devices using a solution of capped ZnO NRs that was stored for almost 400 days (assigned as "Device ZD" in Fig. 9d). The best "ZD" device exhibited an impressive PCE of 3.05% with J_{sc} of 8.61 mA. cm^{-2}, V_{oc} of 0.6 V, and *ff* of 59%. This clearly indicates that under ambient conditions, the NRs remained charged for more than a year without any appreciable decay. Device ZL, which is representative of IPSCs fabricated by employing ZnO NRs from the scale-up reaction (see section S4 of Supporting Information), also exhibited an impressive PCE of 3.18% owing to J_{sc} of 9.48 mA.cm^{-2}, V_{oc} of 0.59 V, and *ff* of 57%.

In order to show that our modifications with capping of ZnO NRs led to the improved charge transfer characteristics of the IPSCs, we conducted Mott-Schottky and electrochemical impedance spectroscopy (EIS) measurements. Mott–Schottky plots were measured in the dark with three electrode assembly and perturbation amplitude of 10 mV in aqueous KCl electrolyte. Donor density and flat band potential (V_{fb}) of ZnO NRs were estimated from the results of Mott-Schottky analysis using the equations used in our previous work. [63] Fig. 10a shows the Mott-Schottky plots for uncapped and capped ZnO NRs. The positive slopes imply *n*-type conductivity in both the cathode buffer layers. From the Mott-Schottky analysis, the V_{fb} values of the uncapped and capped ZnO NRs were determined to be -0.75 V and -0.96 V (*vs*. Ag/AgCl), respectively. The shift in V_{fb} to more cathodic values for the capped ZnO NRs suggests the evolution of free carrier concentration in the material. [64] The increase in flat- band potential to higher negative values can be attributed to shift of the Fermi level in the capped ZnO NRs, approaching the conduction band, as the hydroxylation progresses. This obviously results into higher V_{oc}

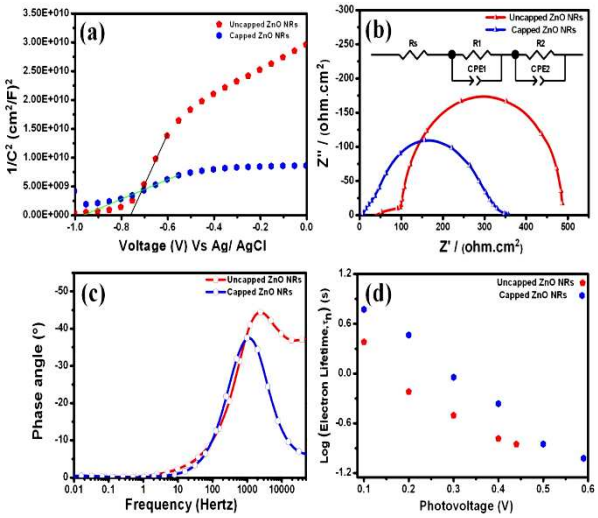

Fig. 10 EIS Analysis; (a) Mott-Schottky plots, (b) Nyquist plots (inset: RC-circuit model), (c) Bode's phase plots, and (d) electron lifetime variation (in the log-linear representation) as a function of photovoltage decay for IPSCs of uncapped and capped ZnO NRs.

Table 3. EIS fitting parameters

ZnO NRs	Rs Ω.cm^2	R1 Ω.cm^2	R2 Ω.cm^2	CPE1-T(F) 10^{-4}	CPE1-P(F)	CPE2-T (F) 10^{-4}	CPE2-P(F)
Uncapped	42.36	79.36	266.83	2.19	0.899	6.19	0.76
Capped	6.5	5.822	40.94	0.33	0.69	3.62	0.54

(0.6 V) in case of IPSCs employing capped ZnO NRs as electron transporting layers. The slope of the linear portions of Mott-Schottky plots is inversely proportional to the dopant density in the films.[65] From the slope of the Mott-Schottky plots in Fig. 10a, the donor density was calculated to be 1.08 x 10^{18} and 6.21 x 10^{19} cm^{-3} for uncapped and capped ZnO NRs, respectively. It is thus obvious that, capping of ZnO NRs was influential to improve the electrical conducting property of cathode buffer by increasing its donor density.

To reveal the differences in the charge transport on the interface between the organic active layer and ITO cathode, ac impedance measurements were carried out on IPSCs using uncapped and capped ZnO NRs as cathode buffer layers. Fig. 10b shows the Nyquist plots for the IPSCs at zero bias under 1 Sun illumination. The Nyquist plots show two distinct semicircles in the frequency regions 10^5~10^3 and 10^2~10^1 Hz. The ac response of semicircle in the high-frequency range was faster than that of the one in the low-frequency range. The semicircle in the high frequency range arise from the cathode buffer (ZnO, in this work), while that in the low frequency range is derived from the organic active layers of P3HT: $PC_{60}BM$. [66] All impedance spectra were fitted to a 2-RC circuit model [32] which contains one resistor and two RC circuits (sub-circuit with a resistor R and a capacitor C in parallel) in series as shown in the inset of Fig. 10b. The symbol CPE, describes the constant phase element of the capacitance, meaning a non-ideal frequency dependent capacitance due to a non-uniform distribution of current by the material

heterogeneity. The elements with subscripts 1 and 2 are related to the capacitance of the interfaces at the semicircles of high and low frequency, respectively, forming a parallel circuit with resistances R_1 and R_2. The R_s represents the ohmic resistance including the electrodes and bulk resistance in the active layer. The parameters determined by the fitting of the experimental data are summarized in Table 3. The R_s, R_1 and R_2 values for IPSCs of uncapped ZnO NRs were estimated to be 42.36, 79.36 and 266.83 $\Omega.cm^2$ respectively. Comparatively, the values of R_s, R_1 and R_2 for IPSCs of capped ZnO NRs were 6.5, 5.82 and 40.94 $\Omega.cm^2$ respectively. Such large decrease in resistances in the latter is attributed to unperturbed charge transportation with lesser recombination centers through highly transparent and conductive capped ZnO NRs. It is thus clear that the diameter of semicircles depends strongly on the nature of ZnO in electron transport layers.

The lifetime of electrons in the IPSCs (τ) can be estimated from the characteristic frequencies of the impedance semicircle at middle frequencies, obtained by plotting Bode phase angle plot, according to the relation $\tau = (1/2\pi f_{max})$, where f_{max} is the maximum frequency of the mid-frequency peak.[67] Fig. 10c shows Bode phase angle versus frequency plots of the IPSC devices based on uncapped and capped ZnO NRs as cathode buffer layers. The corresponding high frequency peak (f_{max}) of the phase angle, related to the charge transfer on the surface of the electrode for uncapped and capped ZnO NRs IPSC devices is located respectively at 2540 and 1137 Hz. Bode's phase angle plot clearly shows that f_{max} is located at lower frequencies for IPSCs of capped ZnO NRs in comparison to that of uncapped ZnO NRs, indicating the increase in electron lifetime. The τ value estimated from Bode's phase plot was found to be 0.062 and 0.139 ms, respectively, for IPSCs of uncapped and capped ZnO NRs, indicating a longer electron lifetime in cathode buffer layers of capped ZnO NRs.

The differences of these cathode buffer layers were further studied by the open-circuit voltage-decay (OCVD) technique which provides a continuous reading of the lifetime as a function of V_{oc}. The electron lifetime (τ_n) in the IPSCs was calculated by fitting the photovoltage decay plot obtained from open-circuit voltage decay measurement and applying an equation developed by Bisquert *et al*.[68] The electron lifetime is given by $\tau_n = -(KT/e)\ (dV_{oc}/dt)^{-1}$, where KT is the thermal energy, e is the positive elementary charge, K is the Boltzmann constant and dV_{oc}/dt is the first-order time derivation of the V_{oc}. Fig. 10d shows the plot of electron lifetime, τ_n (in a log representation), as a function of V_{oc}. It was found that τ_n of the capped ZnO NRs cathode buffer was longer than that of uncapped ZnO NRs, implying a lower charge recombination rate and suggested more efficient electron transfer, which is in accordance with EIS analysis mentioned above. The τ_n of capped ZnO NRs are much higher than those in the uncapped NRs in the low V_{oc} region indicating that capped ZnO NRs possess lower surface trap density and hence reduced charge recombination rates compared with uncapped NRs. The lower surface trap density of capped NRs is consistent with the higher *ff* observed in the IPSCs of capped NRs. Thus, OCVD measurements reveal that lower surface trap density and enhanced electron lifetime for the IPSCs of capped ZnO NRs validate higher PCE than that of uncapped NRs. Because the geometry and configuration are similar for both the devices, it follows that charge transfer across the cathode buffer layer is significantly influenced by the electronic nature of underlying electron collector (uncapped and capped ZnO NRs).

Technical perspective of capping

Capping by acids like MEA typically leaves extra electrons on the nanostructure (in this case NRs). The added electrons occupy delocalized, conduction band-like orbitals in ZnO. These extra electrons have a longer lifetime which obviously aid into effective electron transfer mechanism. Thus, the capping layer ensures selective collection of electrons from the active layer of PSC. Additionally, MEA capping is responsible for hydroxylation of ZnO NRs surfaces. Hydroxylation is typically an example of polar surface configurations. The existence of hydroxylation of outer layers invokes stabilization as well as metallization, an important facet of conductibility.[69] Moreover, as the path for charge transfer is obviously through the medians of ZnO NRs, the increased charge transfer induced by capped ZnO NRs clearly suggest that the ZnO NRs are negatively charged not only from outside but also from the within. Thus, it is no surprise, that the hydroxylated ZnO NRs (i.e. capped) exhibit a colossal enhancement in electrical characteristics.

Conclusions

The capped planar ZnO NRs demonstrate that the modification and deposition process developed by us has tremendous potential of becoming a general approach for fabricating oxidic nanomaterials that can be effectively applied as charge transfer bridges without the use of conventional seed growth methods. As a proof of concept, the IPSCs fabricated using ZnO NRs as cathode buffer layer exhibited a promising PCE of 3.24%, which is the highest reported PCE so far for the configuration of the IPSCs used in this work. The high transparency, improved wettability and enhanced electrical characteristics (conductivity and mobility) owing to hydroxylated ZnO NRs provided by MEA capping resulted in more efficient charge transport followed by an impressive PCE. On the basis of UPS measurements, we attribute this improvement to a substantial reduction in energy barrier on using capped ZnO NRs as cathode buffer instead of uncapped ZnO NRs. In this context, our proposed synthetic strategy opens a new avenue for developing solution-based buffer layers with high degree of functionality and ease of processing. Moreover, capped ZnO NRs exhibited excellent stability in solution for over 400 days. Additionally, high reaction yields in case of prototype as well as scale-up reactions suggest that reaction proceeds in same direction without any undesired and impure byproducts. We envisage that such modified nanomaterials may stimulate the development of polymer solar cells at lower cost and at mass scale.

Acknowledgements

This research was financially supported by the Pioneer Research Center Program through the NRF of Korea funded by the Ministry of Science, ICT & Future Planning (NRF-2013M3C1A3065528) and by a grant from the Program of the Korea Research Institute of Chemical Technology (KRICT), Republic of Korea.

[a]School of Semiconductor and Chemical Engineering, Chonbuk National University, 664-14, 1-ga Deokjin-dong, Deokjin-gu, Jeonju, Jeonbuk, 561-756, Republic of Korea.
[b]Department of Defense Ammunitions, Daeduk College, Daejeon, 305-715, Republic of Korea

[c]Centre for Nanomaterials & Energy Devices, School of Physical Sciences, SRTM, University, 431606, Nanded, India.
[d]Advanced Materials Division, Korea Research Institute of Chemical Technology, Daejeon 305-600, Republic of Korea
*shlee66@jbnu.ac.kr, yoonsch@krict.re.kr, Telephone: +82-63-270-2435 Fax: +82-63-270-2306.

Electronic Supplementary Information (ESI) available: Structural characterizations and supplementary figures (Fig. S1–S5). See DOI: 10.1039/b000000x/

Notes and references

1 N. S. Lewis, *Science,* 2007, **315**, 798.
2 W. U. Huynh, J. J. Dittmer, A. P.Alivisatos, *Science,* 2002, **295**, 2425.
3 B. Liu, H. C. Zeng, *J. Am. Chem. Soc*., 2003, **125**, 4430.
4 W. I. Park, Y. H. Jun, S.W. Jung, G.-C. Yi, *Appl. Phys. Lett.,* 2003, **82**, 964.
5 W. D. Yu, X. M. Li, X. D. Gao, *Appl. Phys. Lett.,* 2004, **84**, 2658.
6 Y. Sun, J. H. Seo, C. J. Takacs, J. Seifter, A. J. Heeger, *Adv. Mater.,* 2011, **23**, 1679.
7 G. Li, C.-W. Chu, V. Shrotriya, J. Huang, Y. Yang, *Appl. Phys. Lett.,* 2006, **88**, 253503.
8 C. Waldauf, M. Morana, P. Denk, P. Schilinsky, K. Coakley, S. A. Chouli, C. J. Brabec, *Appl. Phys. Lett*., 2006, **89**, 233517.
9 M. S. White, D. C. Olson, S. E. Shaheen, N. Kopidakis, D. S. Ginley, *Appl. Phys. Lett*., 2006, **89**, 143517.
10 Q. F. Zhang, C. S. Dandeneau, X. Y. Zhou, G. Z. Cao, *Adv. Mater.,* 2009, **21**, 4087.
11 J. B. Baxter, A. M. Walker, K. van Ommering, E. S. Aydil, *Nanotechnology,* 2006, **17**, S304.
12 E. Galoppini, J. Rochford, H. Chen, G. Saraf, Y. Lu, A. Hagfeldt, G. Boschloo, *J. Phys. Chem. B*., 2006, **110**, 16159.
13 Z. Zhao, H. Liu, S. Chen, *Nanoscale*, 2012, **4**, 7301.
14 D. J. Norris, A. L. Efros, S. C. Erwin, *Science*. 2008, **319***,* 1776.
15 Z. L. Wang, *J. Phys. Condens. Matter.,* 2004, **16**, R829.
16 Z. L. Wang, *Mater. Today*. 2007, **10**, 20.
17 M. Law, L. E. Greene, J. C. Johnson, R. Saykally, P. Yang, *Nat. Mater*. 2005, **4**, 455.
18 Z. L. Wang, J. Song, *Science.* 2006,**312**, 242.
19 A. Tsukazaki, A. Ohtomo, T. Onuman, M. Ohtanin, T. Makino, M. Sumiya, K. Ohtanin, S. F. Chichibu, S. Fuke, Y. Segawa, H. Ohno, H. Koinuma, M. Kawasaki, *Nat. Mater.,* 2005**, 4**, 42.
20 M. Podlogar, J. J. Richardson, D. Vengust, N. Daneau, Z. Samardžija, S. Bernik, A. Recnik, *Adv. Funct. Mater.,* 2012, **22**, 3136.
21 L. Vayssieres, *Adv. Mater.,* 2003, **15**, 464.
22 S. Li, S. Zhou, H. Liu, Y. Hang, C. Xia, J. Xu, S. Gu, R. Zhang, *Mater. Lett.,* 2007, **61**, 30.
23 L. Wang, D. Tsan, B. Stoeber, K. Walus, *Adv. Mater.,* 2012, **24**, 3999.
24 L. Baeten, B. Conings, H.-G. Boyen, J. D'Haen, A. Hardy, M. D'Olieslaeger, J. V. Manca, M. K. V. Bael, *Adv. Mater.,* 2011, **23,** 2802.
25 Q. Yu, W. Fu, C. Yu, H. Yang, R. Wei, M. Li, S. Liu, Y Sui, Z. Liu M. Yuan, G. Zou, G. Wang, C. Shao, Y. Liu, *J. Phys. Chem. C,* 2007, **111**, 17521.
26 D. Chu, W. Y. Masuda, T. Ohji, K. Kato, *J. Am. Ceram. Soc*., 2010, **93***,* 887.
27 R. S. Devan, R. A. Patil, J. –H. Lin, Y.-R. Ma*, Adv. Funct. Mater.,* 2012, **22**, 3326.
28 H. Y. Park, H. Y. Go, S. Kalme, R. S. Mane, S. H. Han, M.Y. Yoon, *Anal. Chem*., 2009, **81**, 4280.
29 T. Ma, M. Guo M., Zhang Y., Zhang, X. Wang, *Nanotechnology,* 2007, **18,** 035605.
30 J. Song, S. Lim, *J. Phys. Chem. C*, 2007, **111**, 596.
31 J. Liu, J. She, S. Deng, J. Chen, N. Xu, *J. Phys. Chem. C,* 2008, **112**, 11685.
32 S. B. Ambade, R. B. Ambade, R. S. Mane G. –W., Lee, S. F. Shaikh, S. A. Patil, O.-S. Joo, S. –H. Han, S. H. Lee, *Chem. Comm.,* 2013, **49**, 2921.
33 C. R. Kagan, D. B. Mitzi, C. D. Dimitrakopoulos, *Science,* 1999, **286,** 945.
34 K. W. Chou, B. Yan, R. Li, E. Q. Li, K. Zhao, D. H. Anjum, S. Alvarez, R. Gassaway, A. Biocca, S. T. Thoroddsen, A. Hexemer, A. Amassian, *Adv. Mater.,* 2013, **25**, 1923.
35 S. Walheim, E. Schaffer, J. Mlynek, U. Steiner, *Science,* 1999, **283**, 520.
36 B. A. Korgel, *Science,* 2004, **303**, 1308.
37 B. E. Sernelius, K. F. Berggren, Z. C. Jin, I. Hamberg, C. G. Graqvist, *Phys. Rev. B,* 1988, **37**, 10244.
38 K. Vanheusden, W.L. Warren, C.H. Seager, D.R. Tallant, J.A. Voigt, B.E. Gnade, *J. Appl. Phys*., 1996, **79** , 7983.
39 D. M. Bagnall, Y. F. Chen, M. Y. Shen, Z.T. Zhu, T. Yao, *J. Cryst. Growth,* 1998, **185**, 605.
40 J. C. Manifacier, J. Gasiot, J. P. Fillard, *J. Phys. E: Sci. Instrum.*, 1976, **9**, 1002.
41 H. W. Choi, K. -S. Lee, T. L. Alford, *Appl. Phys. Lett*., 2012, **101**, 153301.
42 L. Ratke, P. W. Voorhees, Handbook of Growth and Coarsening: Ostwald Ripening in Material Processing. *Springer,* 2002, ISBN 3-40-42563-2, pp. 117.
43 H. S. Song, W. J. Zhang, C. Cheng, Y. B. Tang, L. B. Luo, X. Chen, C. Y. Luan, X. M. Meng, J. A. Zapi-en, N. Wang, C. S. Lee, I. Bello, S. T. Lee, *Crystal Growth & Design*, 2011, **11**, 147.
44 C. Stampfl, C. G. Van de Walle, *Phys. Rev. B,* 1998, **57**, R15052.
45 Y. Yan, G. M. Dalpian, M. M. Al-Jassim, S. H.Wei, *Phys. Rev. B*., 2004, **70**, 193206.
46 X. H. Wu, L. M. Brown, D. Kapolnek, S. Keller, S. P. Den Barrs, J. S. Speck, *J. Appl. Phys*, 1996, **80**, 3228.
47 B. Subash, B. Krishnakumar, M. Swaminathan, M. Shanthi, *Langmuir*, 2013, **29**, 939.
48 C. Gu, C. Cheng, H. Huang, T. Wong, N. Wang, T. Y. Zhang, *Crystal Growth & Design*., 2009, **9**, 3278.
49 A. P. Grosvenor, B. A. Kobe, N. S. McIntyre, *Surface Science*, 2004, **572**, 217.
50 T. C. Damen, S. P. S. Porto, B. Tell, Phys. Rev., 1966, **142**, 570.
51 S. Dhara, S. Chandra, G. Mangamma, S. Kalavathi, P. Shankar, K. G. M. Nair, A. K. Tyagi, C. W. Hsu, C. C. Kuo, L. C. Chen, K. K. Sriram, *Appl. Phys. Lett*., 2007, **90**, 213104.
52 H. M. Cheng, K. F. Lin, H. C. Hsu, W. F. Hsieh, *Appl. Phys. Lett.,* 2006, **88**, 261909.
53 K. Huang, A. Rhys, *Proc. R. Soc. London, Ser*., 1950, **406**, A 204.
54 A. K. Arora, M. Rajalakshmi, T. R. Ravindran, V. Sivasubramanian, *J. Raman Spectrosc.* **2007**, 38, 604.
55 R. Zimmermann, S. Dukhin, C. Werner, *J. Phys. Chem. B,* 2001, **105**, 8544.
56 C. -H. Lin, M. K. Chaudhury, *Langmuir*, 2008, **24**, 14276.
57 D. V. Talapin, C. B. Murray, *Science*, 2005, **310**, 86.
58 A. Gadisa, Y. Liu, E. T. Samulski, R. Lopez, *Appl. Phys. Lett*. **2012**, 100, 253903-1.
59 J. Nelson, J. Kirkpatrick, P. Ravirajan, *Physical Review B* **2004**, 69, 035337.
60 K.; Vandewal, K. Tvingstedt, A. Gadisa, O. Ingan€as, J. Manca, *Nature Mater*., 2009, **8**, 904.
61 M. Wang, Y. Li, H. Huang, E. D.Peterson, W. Nie, W. Zhou, W. Zeng, W. Huang, G. Fang, N. Sun, X. Zhao, D. L. Carroll, *Appl. Phys. Lett*. **2011**, 98, 103305-1.
62 J. F. Hartwig, *Science*, **2002**, 297, 1653.
63 S. M. F. Shaikh, G. Rahman, R. S. Mane, O-S. Joo, *E. Acta.,* 2013, **111**, 593.
64 P. C. Coca, M. Mollar, K. C. Singh, B. Mari, *ECS Journal of Solid State Science and Technology*, 2013, **2 (7)** , Q108.
65 A. J. Bard, R. Memming, B. Miller, *Pure Appl. Chem*., 1991, **63**, 569.
66 T. Kuwabara, C. Iwata, T. Yamaguchi, K. Takahash, *ACS Appl. Mater. Interfaces*, 2010, **2**, 2254.
67 H. Kim, H. Jeong, T. K. An, C. E. Park, K. Yong, *ACS Appl. Mater. Interfaces*. 2013, **5**, 268.
68 J. Bisquert, A. Zaban, M. Greenshtein, Iván Mora-Seró. *J. Am. Chem. Soc.* 2004, **126**, 13350.
69 C. Noguera, J. Goniakowski*, Chem. Rev.,* **2013***,* 113*,* 4073.

